ARTICLE NO. 79-0268R

Measurements of Transition-Front Asymmetries on Ablating Graphite Nosetips in Hypersonic Flight

Daniel C. Reda*
Sandia Laboratories, Albuquerque, N. Mex.
and
Richard M. Raper†
ARO, Inc./AEDC Division, Arnold Air Force Station, Tenn.

Transition experiments were conducted on preablated graphite nosetips in the AEDC Track G facility. Nosetip radius and freestream static pressure were varied to insure transition front movement from sonic-line to stagnation-point proximity. Surface temperature contours were measured with image-converter cameras and results interpreted with interactive graphics to define instantaneous transition front contours. Statistical analyses showed that probability of transition occurrence on any given ray, between the minimum and maximum observed run lengths to transition, was Gaussian. Mean transition front location was observed to progress forward with a power-law dependence on range static pressure; coincidently, transition-front asymmetry, defined by a standard deviation about the mean, was noted to decrease linearly. All results were found to be independent of nosetip radius.

Nomenclature

h	= measured in-plane roughness element height
k	= physical peak-to-valley roughness element height
M	= Mach number
N	= total number of x values in given data set
p	= pressure
Re	= unit Reynolds number, $\rho V/\mu$
$R_N (RN)$	= nosetip radius
s_x	= skewness of x
S	= arc length, measured from stagnation point
T	= temperature
V	= velocity
x	= generalized variable
$\bar{x}$	= arithmetic average of x
$\Delta(x)$	= band width of x
θ	= angle measured along surface from stagnation point
μ	= viscosity
ρ	= density
σ_x	= standard deviation of x
ϕ	= circumferential coordinate

Subscripts

∞	= freestream
max	= maximum
mean	= arithmetic average
min	= minimum
TR	= transition location

Presented as Paper 79-0268 at the 17th Aerospace Sciences Meeting, New Orleans, La., Jan. 15-17, 1979; submitted Jan. 29, 1979; revision received May 7, 1979.

Index categories: Boundary Layers and Convective Heat Transfer—Turbulent; Supersonic and Hypersonic Flow; Entry Vehicle Testing, Flight and Ground.

*Member, Technical Staff, Aerodynamics Dept. Associate Fellow AIAA.

†Project Engineer, von Karman Gas Dynamics Facility. Member AIAA.

I. Introduction

VIABLE techniques for predicting and improving the accuracy of ballistic re-entry vehicles have been actively pursued in recent years. It now has been established that asymmetric nosetip shape change is one of the most influential factors in re-entry-generated contributions to overall strategic system inaccuracies. Aerodynamic forces and moments that act directly on asymmetrically-ablated nosetips, and associated flow distortions that these shapes impose on otherwise axisymmetric afterbody flowfields, can result in re-entry-body trim growth (angle of attack), and possible roll-rate excursions, creating a dispersion of the re-entry vehicle from its predicted ballistic impact point.

Carbonaceous nosetip materials, both graphites and carbon/carbon composites, sublime under high-altitude/laminar-flow conditions, forming a surface microroughness distribution characteristic of each material's composition and fabrication/processing technique. Surface roughness element heights typically span at least an order of magnitude and can thus only be represented in a statistical sense (as will be demonstrated in Sec. II). Surface microroughness elements, as formed during re-entry, create disturbances within the laminar boundary layer; as altitude decreases, Reynolds number increases, and nosetip flowfield conditions capable of amplifying these roughness-induced disturbances are eventually achieved, i.e., transition onset occurs. Boundary-layer transition to turbulence results in more severe heat-transfer rates, increased ablation rates, accelerated shape change, and the formation of a macroroughness pattern downstream of transition (e.g., striations, grooves, and/or scallops).

Transition initially occurs on the nosetip in the vicinity of the sonic line, $(S/R_N) \cong 0.7$, and progresses forward at a rate dependent on both the material surface roughness and the re-entry vehicle trajectory. Under some conditions, this forward progression occurs rapidly, and a rather symmetric/biconic nosetip shape results. However, under conditions where the leading edge of the transition zone remains removed from the stagnation point throughout any appreciable portion of the trajectory, a laminar island forms, followed by an indented/turbulent-flow region.

Since the surface microroughness distribution is statistical in nature, so then must transition be described (modeled) in a

probabilistic sense, i.e., there exists a probability that transition will occur at a specified distance along each ray emanating from the nosetip stagnation point. Asymmetric transition fronts thus result, and are the driving potential for asymmetric nosetip shape change. Figure 1 shows an example of an asymmetric nosetip shape, formed during a re-entry flight test[1] of an initially hemispherical graphite nosetip, which illustrates these points.

A procedure for the calculation of asymmetric nosetip shape change during re-entry, based on the above-described phenomenological arguments, was recently formulated by Dirling.[2] This procedure, when mathematically coupled with predictions of resulting vehicle aerodynamics,[3,4] allows for the probabilistic calculation of re-entry-body trim growth on any specified trajectory. A statistically large number of computer runs could be made for each of several trajectories bracketing a missile system's operating envelope, thereby analytically defining nosetip-induced contributions to the system's overall circular error probability. Further, such an exercise could be conducted for a total cost significantly below that of even a single flight test.

As promising as such a technique appears, certain key elements in the procedure remain to be proven. Of critical importance is the "transition law" utilized. Obviously, for nosetip shape-change history to be predicted accurately, a code must realistically model "the statistics" of transition onset, and transition front location, on each ray considered, as a function of the ablated material surface microroughness distribution, ablation (blowing) rate, wall-temperature ratio, Reynolds number, etc.

To date, the re-entry community has relied on one primary data source for generation of correlations aimed at modeling transition onset/location on re-entry vehicle nosetips (e.g., see Fig. 2 of Ref. 2). This data base was obtained on nonporous, metallic, thin-skinned calorimeter models, of various *uniform* surface roughness scales, exposed to Mach 5 wind tunnel environments. No information concerning the asymmetric nature of transition was, therefore, generated. Further, techniques and results outlined in Refs. 5 and 6 raised some questions concerning the extrapolation of a nosetip boundary-layer transition correlation, based on the aforementioned wind tunnel data, to an actual nosetip material exposed to hypersonic, clear-air environments.

The primary objective of the present research effort was, therefore, to investigate experimentally and to define empirically the asymmetry characteristics of transition fronts on ablating graphite nosetips exposed to hypersonic clear-air environments; results so generated would also serve to expand the data base necessary for the generation of an improved correlation for "mean" boundary-layer transition front location as a function of "average" roughness element height and gasdynamic/flowfield parameters.

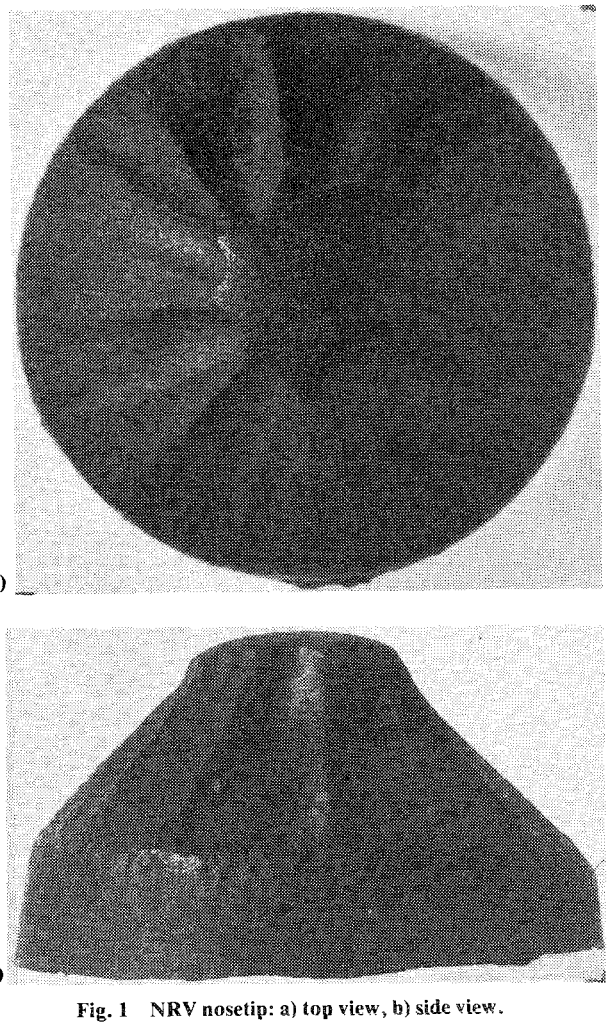

Fig. 1 NRV nosetip: a) top view, b) side view.

II. Experimental Procedures

In order to create the characteristic microroughness distribution for any particular material of interest, nosetips of that material are exposed to a low-pressure/high-enthalpy environment generated in an arcjet facility, thereby simulating the high-altitude laminar-ablation regime experienced in flight. Sufficient ablation within the sublimation regime must be experienced in order to remove any trace of the material's initial (as machined) surface finish.

In order to quantify this surface roughness distribution for each material, at least one post-test ablation model is mounted and sectioned, and the cross-sectioned plane progressively polished to expose the as-ablated surface details. A statistically large number of individual roughness elements are then measured via microscopy.[7]

Figure 2 shows surface microroughness characterization results for CMT graphite, an intermediate grain-size bulk graphite used in the present experiment. In this case, two nosetips were sectioned and roughness elements measured along three rays of each one, for a total data population of 350 individual elements. The mean, standard deviation, and skewness of this data set were calculated according to Eqs. (1-3) here written in terms of a generalized variable x:

$$\bar{x} = \frac{1}{N} \sum_{i=1}^{N} x_i \tag{1}$$

$$\sigma_x = \left[\frac{1}{N} \sum_{i=1}^{N} (x_i - \bar{x})^2 \right]^{1/2} \tag{2}$$

$$s_x = \frac{1}{N} \sum_{i=1}^{N} (x_i - \bar{x})^3 \tag{3}$$

Comparison was made with a Gaussian distribution, defined by

$$\mathrm{PO} = \left[\frac{\Delta(x)}{\sqrt{2\pi}\sigma_x} \right] e^{(-1/2\sigma_x^2)(x-\bar{x})^2} \tag{4}$$

Probability of occurrence (PO) values for each bandwidth were integrated to form cumulative probabilities (CP) and thus probabilities of exceedence (PE = 1 − CP). Reasonable agreement with a Gaussian distribution in PE vs h coordinates, was noted.

Using equations reported by Dirling,[7] the mean and standard deviation for the h distribution were transformed to physical peak-to-valley quantities, assuming hemispherically shaped elements: $\bar{k} = 9.73\ \mu$ (0.383 mils), $\sigma_k = 5.59\ \mu$ (0.220 mils).

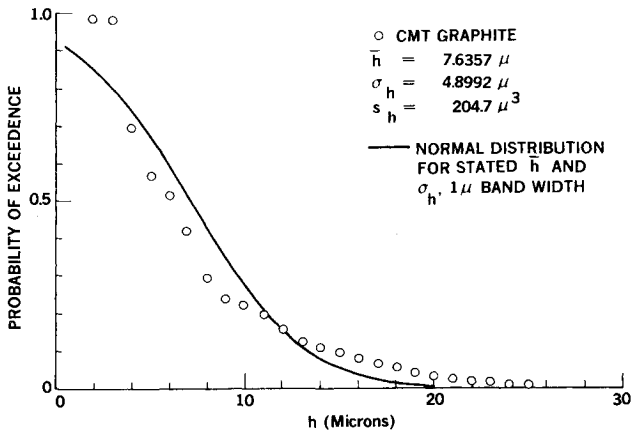

Fig. 2 Microroughness distribution.

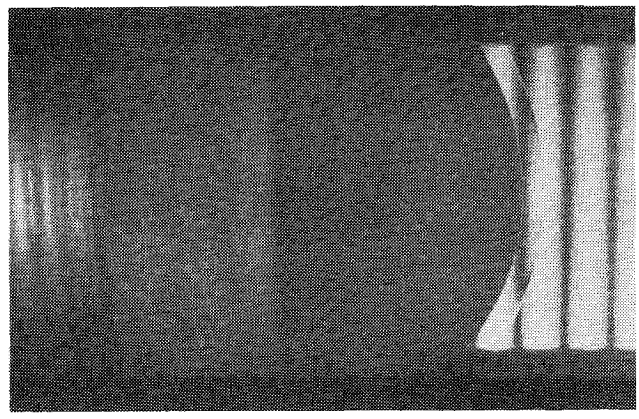

Fig. 3 Side-view laser photograph.

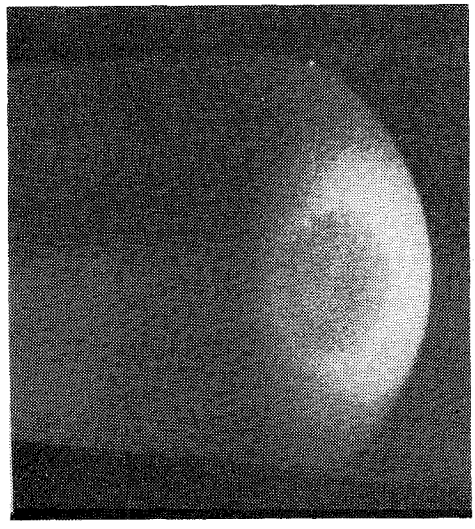

Fig. 4 Oblique-view laser photograph.

The influence of such a surface roughness distribution on nosetip boundary-layer transition is determined in the following manner.[5,6] Preablated nosetips are mounted on ballistics-range models and launched at hypersonic velocity into well-defined clear-air environments. Nosetip surface temperature distributions are measured at various stations along each range trajectory, from which boundary-layer transition zone presence, location, and degree of asymmetry can be ascertained (as will be illustrated in Sec. III). Measurements of nosetip surface temperature distributions are made with an instrument called an image-converter camera; the overall measurement technique is termed electro-optical pyrometry. The basic operating principle of this technique is to record, on film, images of known temperature sources (filtered and unfiltered views of a carbon-arc electrode) and the image of an unknown temperature source (the nosetip); application of the resulting calibration relationship between source brightness temperature and film density allows temperature distributions on the unknown temperature source to be determined. The instrument used to read and digitize film-density levels, i.e., surface-temperature levels, is termed an isodensitometer.

All ballistics range testing of this type is now conducted in Range G of the Arnold Engineering Development Center (AEDC). With successful implementation of a guided-track system,[8] this facility offers some distinct advantages over freeflight testing, without compromising achieveable aerothermodynamic environments. Since the rail system generates zero-dispersion/low-angle-of-attack trajectories, instrumentation can be placed closer to the model "flight" path, yielding better resolution and lower viewing angles (for more nearly end-on views). Gas-cap radiation can be quenched locally, at each surface temperature measurement station, by continuously purging a small volume of the test core with an inert gas (helium); this capability eliminates data attenuation by the gas cap and allows for lower-threshold surface-temperature measurements to be made. In addition to these advantages, a model-recovery capability has been achieved; after traversing the various data acquisition stations located along the 305 m track, the model is guided into a 152 m long recovery tube and is decelerated to rest through compression of an inert volume of gas.

The two largest nosetip-radius models utilized in the present program ($R_N = 2.29$ and 3.18 cm) incorporated a new and important feature. Small cylindrical "pins" or protuberances, comprised of a carbon/carbon composite, were placed at a precise radial distance from the nosetip centerline (well downstream of the sonic-line location), every 90 deg in the circumferential coordinate. Aerodynamic heating renders these markers visible to the image-converter cameras, thereby providing a precise definition of the nosetip stagnation point on resulting data negatives; because of the pins' location relative to the sonic line, upstream influence is negligible, and transition-zone-asymmetry data are not compromised by their presence.

Figure 3 shows a side-view laser photograph of one model undergoing clear-air testing on the Range G track system. Details of the nosetip bow shock were made visible by use of a striped background screen; measurements of shock standoff distances taken from such photographs were found to be in nominal agreement with values predicted by a state-of-the-art nosetip shape-change code.[9] Figure 4 shows a front-lighted/oblique-view laser photograph of one nosetip surface; such photographs were used to screen all data shots for potential surface defects caused by launch loads and/or occasional particle impacts.

Figure 5 shows image-converter camera photographs of preablated CMT graphite nosetips launched at 4877 m/s into air at static pressures from 0.164 to 0.395 atm. The relatively cool (dark) center of each nosetip image corresponds to a region of laminar flow, while the relatively hot (white) region encircling it defines a zone of transitional/turbulent flow heat transfer. As can be seen, the leading edge of the transition zone progressed forward with increasing static pressure (i.e., with decreasing effective altitude).

As noted, each image-converter negative must be scanned by an isodensitometer in order to define relative film densities, and thus nosetip surface temperature levels. This procedure has now been automated at AEDC such that, once a reference point (i.e., the stagnation point as defined by the marker pins) is set on the nosetip image, film density can be read and digitized, and a surface temperature level calculated,

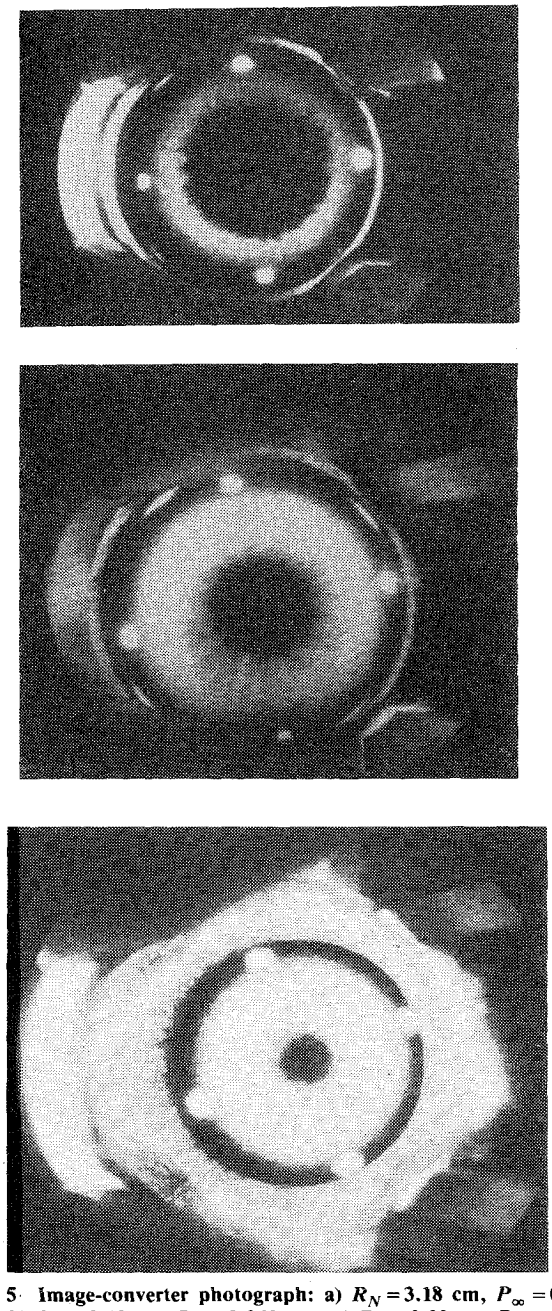

Fig. 5 Image-converter photograph: a) $R_N = 3.18$ cm, $P_\infty = 0.164$ atm, b) $R_N = 3.18$ cm, $P_\infty = 0.263$ atm, c) $R_N = 2.29$ cm, $P_\infty = 0.395$ atm.

at each point within a preselected nosetip surface coordinate system. At present, a data point is taken every 3 deg in the arc length (S/R_N) or θ coordinate, with 120 individual rays being scanned, one every 3 deg in the circumferential (ϕ) coordinate. The camera view angle (5 deg) is compensated for in the preprogrammed software used to position the isodensitometer sensing area. All data points so reduced were stored on magnetic tape for subsequent analyses.

III. Data Interpretation/Analysis

All surface-temperature data were read into a CDC 6500 computer, which was linked to a CDC 240 series GRID (Graphics Remote Interactive Display). Data interpretation/analysis[10] was then implemented by submitting a program which called the data from storage and activated the GRID terminal. Average and individual radial surface temperature distributions could thus be displayed for each image-converter camera station utilized in data acquisition.

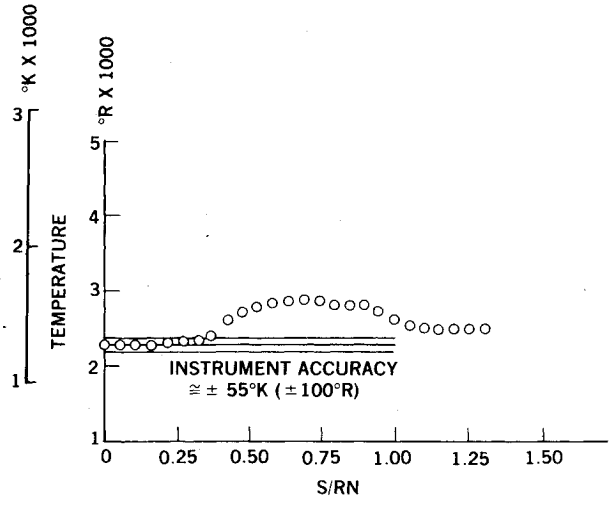

Fig. 6 Typical radial surface temperature distribution.

Average surface temperature distributions vs (S/R_N) or θ could be generated and displayed simply by arithmetically averaging 120 surface temperature measurements at each surface coordinate value. Such distributions, when obtained at each of several stations along a known trajectory, can be utilized for nosetip thermal response code validation via comparisons of predicted and measured results (both being simultaneously displayed; this topic, however, will not be addressed in the present paper).

Figure 6 shows an example of an individual radial surface temperature distribution as displayed on the GRID screen. A transition point was inferred along each such ray by noting the location on the (S/R_N) coordinate where the surface temperature curve underwent a positive change in slope. In practice, this value was recorded by positioning a tracking cross with a light pen at the desired location on the GRID screen and hitting a specific key on the terminal. The locus of all such points (120 maximum) defines the instantaneous transition-front contour on the nosetip surface.

After interpretation, a matrix of ϕ and $(S/R_N)_{TR}$ values for each station is stored on tape for subsequent statistical analyses; results can be recalled, displayed, and plotted in various coordinates, as will be illustrated in the next section.

IV. Results

Test conditions for the chosen material were selected so as to yield transition-front locations which would span the entire regime of interest, from sonic-line proximity to stagnation-point proximity. In addition, nosetip radius and test gas were varied in order to ascertain any sensitivity of the results to absolute nosetip size and/or the presence of mass addition (ablation in the oxidation regime vs no ablation). Ranges of all test variables are outlined as follows: $V_\infty = 4877$ m/s (16,000 ft/s), $T_\infty = 300$ K (540 °R), $M_\infty = 14.0$, $P_\infty = 0.132$-0.395 atm, $Re_\infty = 2.85\text{-}8.53 \times 10^5$/m ($0.87\text{-}2.60 \times 10^5$/ft), $R_N = 1.02$,‡ 2.29, 3.18 cm, as measured on the ablated profiles, gas = air, nitrogen.

Figures 7-10 are representative of all results pertinent to the present paper. These data, for $(S/R_N)_{TR,\ \text{mean}} \cong 0.4$, were plotted directly from the various GRID displays utilized in data analysis. It should be noted that all data presented herein were obtained prior to any significant rearward movement, or "breakup," of the transition front. This phenomenon was observed on some trajectories at "late time," due either to a reduction in instantaneous stagnation pressure on the nosetip, i.e., model deceleration, or to an appreciable rise in model wall temperature, i.e., increased stability of the laminar boundary layer (?), or both. Such results may prove useful in

‡No marker pins, therefore yielded mean data only.

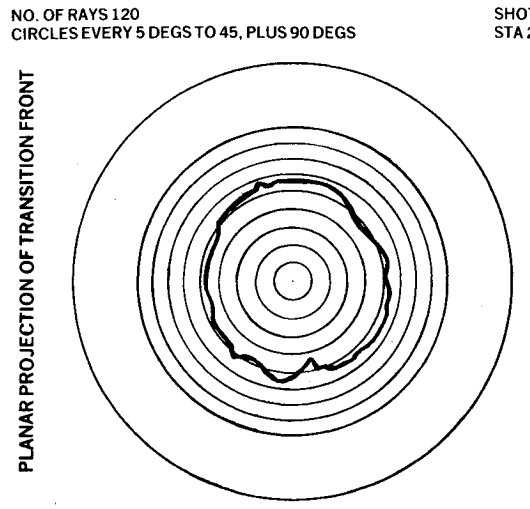

Fig. 7 Planar projection of transition front.

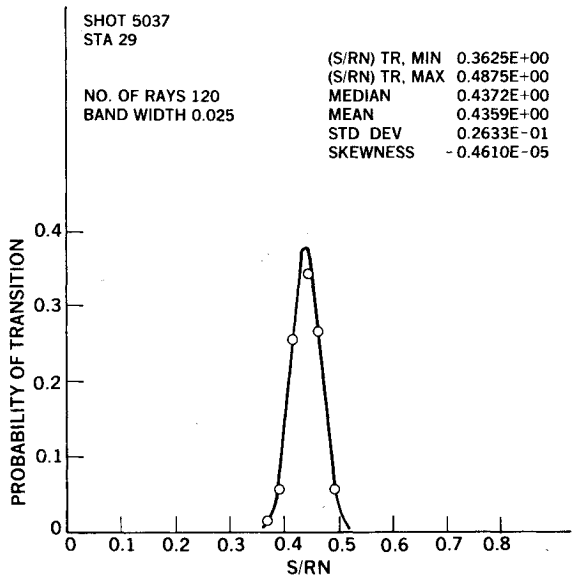

Fig. 8 Probability of transition occurrence.

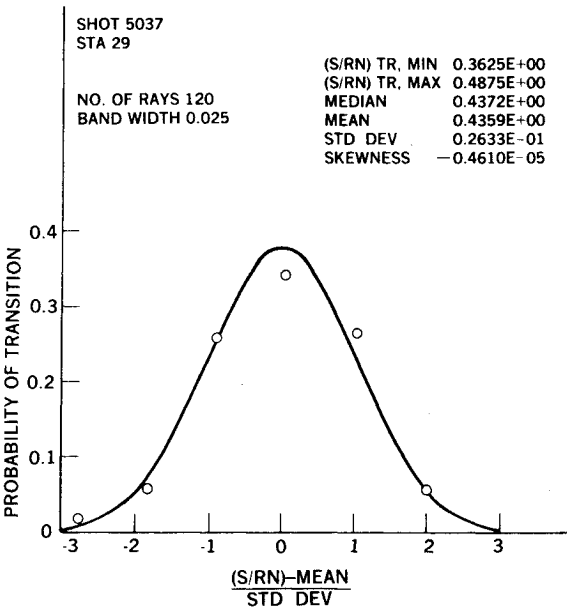

Fig. 9 Probability of transition occurrence.

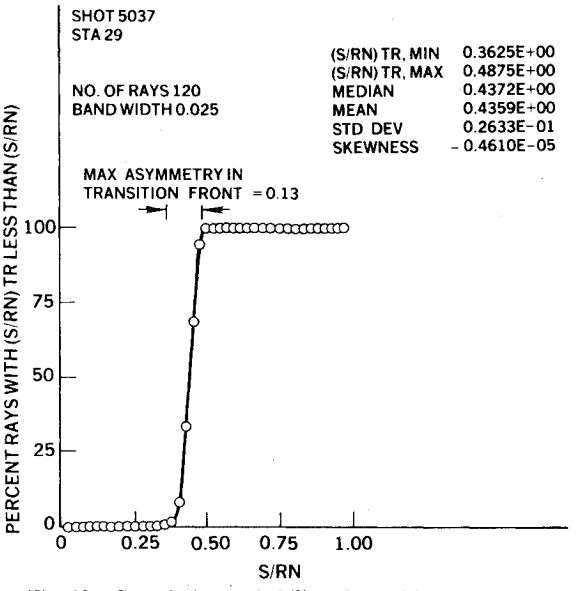

Fig. 10 Cumulative probability of transition occurrence.

defining incipient transition "onset" conditions, a subject apart from the present paper.

Figure 7 shows a planar projection of the transition front and Fig. 8 shows the probability of transition occurrence vs (S/R_N). The solid line is the normal (or Gaussian) distribution corresponding to the experimentally-defined mean and standard deviation of this 120-point data set. Transition location data are displayed for an (S/R_N) band width of 0.025, a value defined by the "reasonable" limit to which inflection-point locations could be read from the radial surface temperature distributions (i.e., a band width equal to $\simeq$ ½ the spacing between individual data points; recall Fig. 6).

Figure 9 shows the probability of transition occurrence as a function of the nondimensionalized Gaussian coordinate, from -3 to $+3$ standard deviations about the mean.

Figure 10 shows the plot obtained by integrating the results of Fig. 8, i.e., cumulative probability of transition occurrence vs (S/R_N).

While not all comparisons of the data with a Gaussian distribution showed such an excellent level of agreement as witnessed in Figs. 8-10, the data, in general, did show maximum probabilities of transition occurrence to exist near the mean location, with a fairly uniform/symmetric decrease of the probability to either side of the mean. Hence, for purposes of modeling transition-front asymmetries on CMT graphite nosetips, the following statement is offered: the probability of transition occurrence on any given ray, between the minimum and maximum observed run lengths to transition, was found to be well approximated by a Gaussian distribution.

Figures 11-14 were generated in an attempt to describe empirically both the mean transition-front behavior and the degree of transition-front asymmetry in terms of directly measurable quantities. Figures 11 and 12 show the mean transition-front location as a function of freestream static pressure in both linear and logarithmic coordinates. As can be seen, the mean transition-front location progressed forward, from sonic-line proximity to stagnation-point proximity, with a power-law dependence on freestream static pressure. Within the spread of present data, no dependence of the mean location on either nosetip radius or mass addition was noted.

Two parameters were utilized in the present study to characterize transition-front asymmetry: a standard deviation about the mean, σ_{TR}, calculated via Eq. (2) and the maximum transition-front asymmetry, calculated as the difference

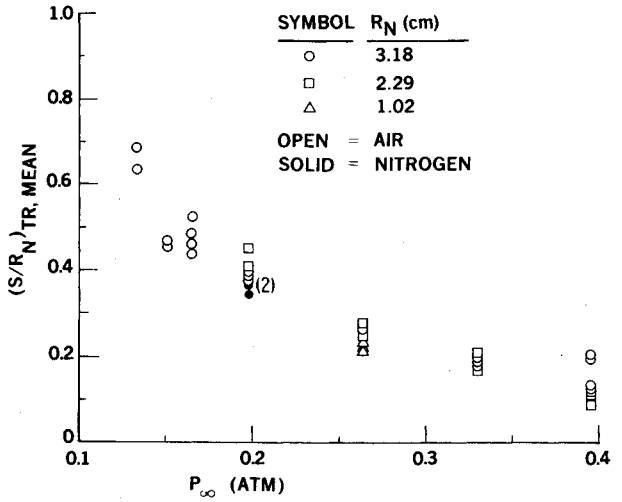

Fig. 11 Mean transition-front location vs freestream static pressure.

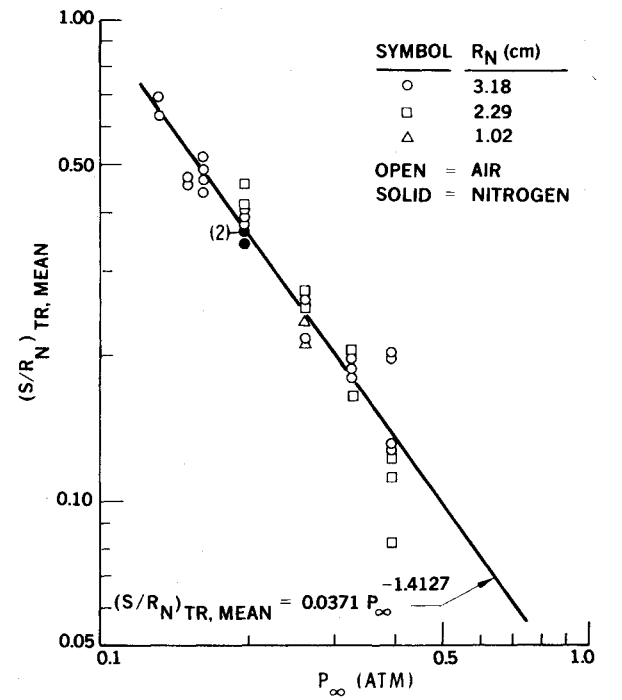

Fig. 12 Mean transition-front location vs freestream static pressure.

between the maximum and minimum observed run lengths to transition. Figures 13 and 14 present results in terms of these two parameters, respectively, each plotted as a function of measured mean transition-front location.

It was noted that as the transition front progressed forward, its degree of asymmetry, defined by either σ_{TR} or maximum transition-front asymmetry, linearly decreased; linear least-squares fits, with nonzero and forced-zero intercepts, were both found to give a reasonable empirical description of the data. Measured maximum transition-front asymmetry values were found to be of the order of 4.2 to 4.6 times σ_{TR}, i.e., they were distributed ± 2.1 to ± 2.3 standard deviations about the mean, thereby encompassing 96 to 98% of all possible values normally distributed. As was the case for mean transition-front behavior, no dependence of transition-front asymmetry on nosetip radius or ablation rate was noted. It should be noted in closing that present experimental techniques could be applied to obtain similar empirical representations of transition-front asymmetries on nosetips comprised of other candidate materials.

V. Conclusions

An experimental effort was undertaken to investigate and empirically define the asymmetry characteristics of transition fronts on ablating graphite nosetips exposed to hypersonic clear-air environments. Measurements of nosetip surface-temperature distributions, and the interpretation of these

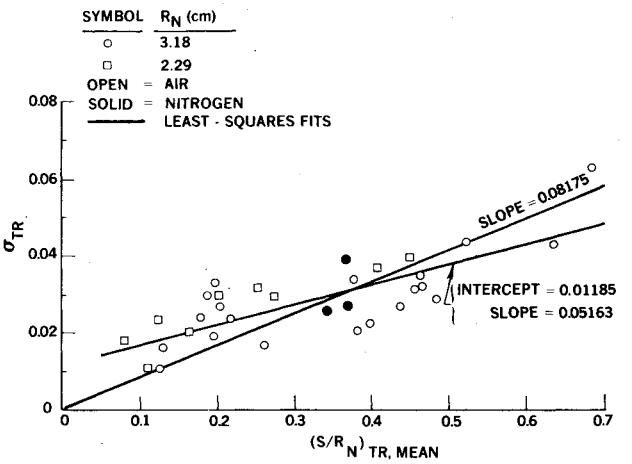

Fig. 13 Transition-front asymmetry, standard deviation vs mean location.

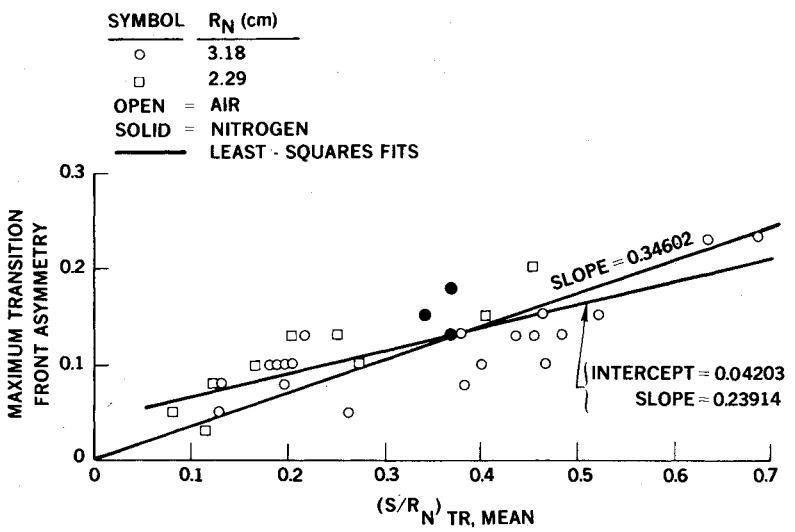

Fig. 14 Maximum transition-front asymmetry vs mean location.

results to define instantaneous transition-front contours, lead to the following observations.

1) The probability of transition occurrence on any given ray, between the minimum and maximum observed run lengths to transition, was found to be well approximated by a Gaussian distribution.

2) The mean transition-front location was observed to progress forward, from sonic-line proximity to stagnation-point proximity, with a power-law dependence on freestream static pressure, i.e., on freestream unit Reynolds number.

3) As the transition front progressed forward, its degree of asymmetry, as defined by a standard deviation about the mean location, was observed to decrease linearly.

4) No dependence of either the mean transition-front location, or its degree of asymmetry, on nosetip radius or ablation rate was observed.

Acknowledgments

This research was sponsored through the Re-entry Technology Program Office, Naval Surface Weapons Center, White Oak Laboratory, with W. Carson Lyons, Jr. serving as Program Coordinator. The expert assistance of Hensel S. Brown, mathematician, N.S.W.C./W.O.L., is gratefully acknowledged.

References

[1]English, E. A., "Nosetip Recovery Vehicle Postflight Development Report," Sandia Laboratories, Albuquerque, N. Mex., Technical Rept. SAND75-8059, Jan. 1976.

[2]Dirling, R. B., Jr., "Asymmetric Nosetip Shape Change During Atmospheric Entry," AIAA Paper 77-779, June 1977; also *AIAA Progress in Astronautics and Aeronautics-Aerodynamic Heating and Thermal Protection Systems*, Vol. 59, edited by L. S. Fletcher, New York, 1978, pp. 311-327.

[3]Swain, C. E., "Aerodynamics of Re-Entry Vehicles with Asymmetric Nosetip Shape Change," AIAA Paper 77-782, Albuquerque, N. Mex., June 1977.

[4]Hall, D. W. and Nowlan, D. T., "Aerodynamics of Ballistic Re-Entry Vehicles with Asymmetric Nosetips," AIAA Paper 77-701, Albuquerque, N. Mex., June 1977; also *Journal of Spacecraft and Rockets*, Vol. 15, Jan.-Feb. 1978, pp. 55-61.

[5]Reda, D. C., Leverance, R. A., and Longas, S. A., "Aerothermodynamic Testing and Analyses of Re-Entry Vehicle Nosetips in Hypersonic Ballistics-Range Flight," *22nd International Instrumentation Symposium*, Instrument Society of America, San Diego, Calif., May 1976.

[6]Reda, D. C. and Leverance, R. A., "Boundary-Layer Transition Experiments on Preablated Graphite Nosetips in a Hyperballistics Range," *AIAA Journal*, Vol. 15, March 1977, pp. 305-306.

[7]Dirling, R. B., Jr., "On the Relation Between Material Variability and Surface Roughness," AIAA Paper 77-402, San Diego, Calif., March 1977.

[8]Norfleet, G. D., Hendrix, R. E., and Jackson, D., "Development of a Hypervelocity Track Facility at AEDC," AIAA Paper 77-151, Los Angeles, Calif., Jan. 1977.

[9]Rafinejad, D., Dahm, T. J., Brink, D. F., Abbett, M. J., and Wolf, C. J., "Inviscid Flow and Heat Transfer Modeling for Re-entry Vehicle Nosetips," Space and Missile Systems Organization, SAMSO-TR-77-11, Vol. I, Oct. 1976.

[10]Reda, D. C. and Brown, H. S., "Analysis of Nosetip Boundary-Layer Transition Data Utilizing Interactive Graphics," *24th International Instrumentation Symposium*, Instrument Society of America, Albuquerque, N. Mex., May 1978.